On the magnetorotational instability in relativistic hypermassive neutron stars

Daniel M. Siegel,[1] Riccardo Ciolfi,[1] Abraham I. Harte,[1] and Luciano Rezzolla[1]

[1]*Max Planck Institute for Gravitational Physics (Albert Einstein Institute)*
Am Mühlenberg 1, 14476 Potsdam-Golm, Germany
(Dated: February 19, 2013)

A differentially rotating hypermassive neutron star (HMNS) is a metastable object which can be formed in the merger of neutron-star binaries. The eventual collapse of the HMNS into a black hole is a key element in generating the physical conditions expected to accompany the launch of a short gamma-ray burst. We investigate the influence of magnetic fields on HMNSs by performing three-dimensional simulations in general-relativistic magnetohydrodynamics. In particular, we provide direct evidence for the occurrence of the magnetorotational instability (MRI) in HMNS interiors. For the first time in simulations of these systems, rapidly-growing and spatially-periodic structures are observed to form with features like those of the channel flows produced by the MRI in other systems. Moreover, the growth time and wavelength of the fastest-growing mode are extracted and compared successfully with analytical predictions. The MRI emerges as an important mechanism to amplify magnetic fields over the lifetime of the HMNS, whose collapse to a black hole is accelerated. The evidence provided here that the MRI can actually develop in HMNSs could have a profound impact on the outcome of the merger of neutron-star binaries and on its connection to short gamma-ray bursts.

Introduction. The magnetorotational instability (MRI) refers to exponentially growing modes that can develop in differentially rotating magnetized fluids [1], and is believed to play a pivotal role in a variety of astrophysical systems. Various analytic and numerical studies agree that through the generation of turbulence, the MRI is the main mechanism for the outward transport of angular momentum in accretion disks around compact objects [2]. The MRI can also play a role in core-collapse supernovae, either by powering the explosion through the conversion of rotational energy into magnetic energy and the production of a magnetohydrodynamic (MHD) outflow [3], or as a source of thermal energy generated by the MRI-induced turbulence and adding to a neutrino-driven explosion [4, 5]. Finally, MRI effects are particularly important when modelling high-energy supernovae and hypernovae [5].

Here we consider a further scenario where the MRI may play a crucial role: the evolution of hypermassive neutron stars (HMNSs). HMNSs are metastable objects that can be formed by the merger of neutron star binaries [6, 7]. They are differentially-rotating neutron stars which exceed the mass limits of rigidly rotating stars. The eventual collapse of a HMNS – induced either by neutrino cooling [8], or by the removal of differential rotation via magnetic fields [9], fluid viscosity or gravitational radiation [7] – leads to a spinning black hole surrounded by a hot and dense torus. The evolution of magnetic fields in HMNSs is of great importance since their rearrangement following amplification by magnetic winding and the MRI may provide the necessary conditions to launch the relativistic jets observed in short gamma-ray bursts (SGRBs) [9–12].

Numerical simulations of the MRI face a fundamental challenge: The wavelength of the fastest growing mode of the instability is proportional to the magnetic field strength and is typically much smaller than the scale of the astrophysical system considered. Due to computational limitations, many simulations therefore fail to resolve the MRI unless very high initial magnetic fields are employed, or only a small part of the system is simulated as in local or semi-global simulations (e.g. [13–15]), or the number of spatial dimensions is reduced via symmetries (e.g. [10, 16–18]). In addition, most simulations attempting to resolve the MRI were conducted within Newtonian or special-relativistic MHD. The most advanced general-relativistic results on the MRI in HMNSs date back to the exhaustive work of [10, 16], where the system was studied in axisymmetry and a specific stage of the magnetic-field amplification was interpreted as evidence for the MRI.

Here, we focus on the pre-collapse phase of the HMNS evolution and provide evidence for the occurrence of the MRI in global, three-dimensional and fully general-relativistic MHD simulations. The emergence of well-resolved coherent channel flows allows us to measure quantities such as the wavelength and the growth rate of the fastest growing mode, opening the way to a systematic study of the MRI in HMNSs.

Numerical setup. As a typical HMNS, we consider the axisymmetric initial model A2 of [19], which is constructed using the RNS code [20]. This assumes a polytropic equation of state (EOS) $p = K\rho^\Gamma$, where p denotes the fluid pressure and ρ the rest-mass density, with $K = 100$ (in units where $c = G = M_\odot = 1$) and $\Gamma = 2$. The initial HMNS has an ADM mass of $M = 2.23 \, M_\odot$ and is differentially rotating according to a "j-constant law" with central angular velocity $\Omega_c = (u^\phi/u^t)_c = 2\pi \times 7.0$ kHz, where u^μ is the fluid 4-velocity. On top of this purely hydrodynamic equilibrium model, we add a poloidal magnetic field confined inside the star and specified by the vector potential $A_\phi = A_b \varpi^2 \max\{(p - 0.04 \, p_{max}), 0\}$, where ϖ denotes the cylindrical radius and p_{max} the maximum fluid pressure [9]. We tune A_b so as to have central magnetic fields $B_c^{in} = (1 - 5) \times 10^{17}$ G. Despite the very high resolutions employed here, such strong magnetic fields are essential to resolve the MRI. Even at these strengths, however, the average magnetic-to-fluid pressure ratios in these models are only $(0.045 - 1.2) \times 10^{-2}$.

Our simulations are performed with the Whisky [21] and

the `Ccatie` codes [22]. These solve the coupled Einstein-MHD equations in 3+1 dimensions on a Cartesian grid employing high-resolution shock-capturing schemes and the conformal traceless decomposition of the ADM formulation of the Einstein equations (see [9] for details). The fluid is assumed to follow ideal MHD and the ideal-fluid EOS $p = (\Gamma - 1)\rho\epsilon$, where ϵ is the specific internal energy and $\Gamma = 2$. The computational grid comprises a spatial box of dimensions $[0, 94.6] \times [0, 94.6] \times [0, 53.9]$ km with four mesh-refinement levels [23] and a fiducial finest resolution with coordinate grid spacing $h = 44$ m. This is comparable to the $h \simeq 37$ m used in previous simulations (which, however, assumed axisymmetry) [10, 16]. All of the results presented here originate from a spatial region that is entirely confined to the finest refinement level. To reach high enough spatial resolutions and make these calculations possible at all, we employ a reflection symmetry across the $z = 0$ plane and a $\pi/2$ rotation symmetry around the z-axis. Repeating some simulations with π symmetry does not alter results found by assuming $\pi/2$ symmetry. The z-symmetry provides large computational savings, but suppresses the toroidal field in the equatorial plane and this could alter the evolution. However, low-resolution simulations in [11] without the z-symmetry do not hint to this.

Analytical predictions. In our initial axisymmetric configuration, magnetic fields are purely poloidal while the fluid velocity is purely toroidal. The fluid does not rotate uniformly along magnetic field lines, so the magnetic field is "wound up" as the HMNS rotates. Assuming axisymmetry and a sufficiently slow variation of the 3-metric γ_{ij}, of the poloidal magnetic field and of the angular velocity, the induction equation can be used to show that

$$B_{\text{tor}} \approx (\varpi B^i \partial_i \Omega) t = a_{\text{w}} t. \tag{1}$$

Here, $B_{\text{tor}} = \gamma_{ij} B^i e_\phi^j$, where e_ϕ^i is the unit vector proportional to the azimuthal Killing field. The linear-in-time growth is expected only during the first phase of the evolution.

There exists no adequate theoretical description of the MRI in systems of the type considered here. Nevertheless, we observe effects similar to those known to arise in simpler systems like accretion disks. In particular, certain short-wavelength modes appear to be preferentially amplified over time. From a linear perturbation analysis of the Newtonian MHD equations for axisymmetric perturbations, the characteristic timescale and wavelength for the fastest growing mode with wave vector k_{MRI}^i may be estimated by [2]

$$\tau_{\text{MRI}} \sim \Omega^{-1}, \qquad \lambda_{\text{MRI}} \sim \left(\frac{2\pi}{\Omega}\right)\left(\frac{B_i e_k^i}{\sqrt{4\pi\rho}}\right) \tag{2}$$

on an order-of-magnitude level, where e_k^i is the unit vector along k_{MRI}^i. Note that τ_{MRI} is independent of B while λ_{MRI} is linear in it. If these estimates are approximately valid for our system, they can only be expected to hold in an appropriate "inertial frame." As the 4-metric $g_{\mu\nu}$ is significantly different from the flat spacetime one, the estimate for λ_{MRI} needs to be corrected by a factor $\sqrt{-g_{00}}$ (which can be quite far from unity). Ignoring this correction can easily lead to inappropriate estimates for the numerical resolution required to resolve
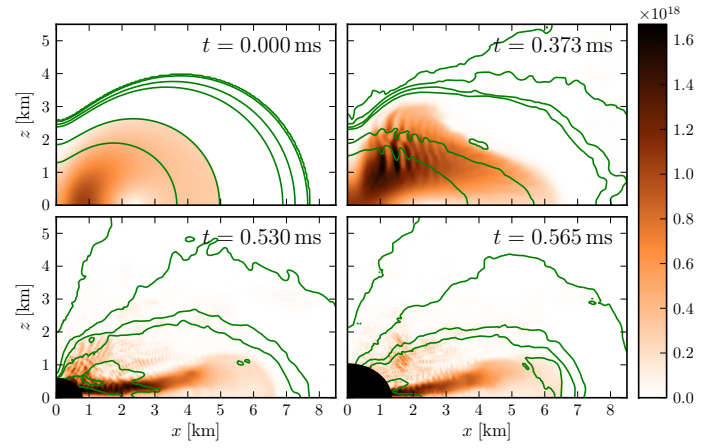

FIG. 1. Rest-mass density contours ($\rho = 10^j$ g/cm^3 with $j = 15.7, 15, 14.7, 14, 13.7, 12.7$, and 11) and the norm of the magnetic field in G in the (x, z) plane at four representative times. The region inside the horizon is masked for reasons of clarity.

the MRI. Converting between coordinate and inertial quantities, τ_{MRI} is changed by the same factor as Ω^{-1}. The first estimate of Eq. (2) is therefore preserved as-is.

Numerical results. Figure 1 shows a section in the (x, z) plane for our fiducial simulation (i.e. with $B_c^{\text{in}} = 5 \times 10^{17}$ G) in terms of the color-coded norm of the magnetic field and selected density contours for four characteristic stages of the evolution. These are: the initial configuration, which shows a highly flattened HMNS due to rapid rotation; the stage of pronounced MRI development indicated by the ripples in the magnetic field and the rest-mass density; the time of collapse to a black hole, when the apparent horizon is formed; the early post-collapse phase with a magnetized and geometrically thick torus being formed in the vicinity of the black hole. We concentrate here only on the MRI in the interior of HMNSs, leaving the discussion of the potential development of the MRI in the torus to Ref. [11] and to future work.

In order to investigate the properties of the MRI in detail and since the system at the stage of MRI development is still essentially axisymmetric, we restrict to a two-dimensional region in the meridional plane defined by $(x, z) \in [1.0, 3.0] \times [1.0, 2.3]$ km, where the MRI is seen most prominently and which has the typical dimensions of local Newtonian MRI simulations. In the upper panel of Fig. 2 we report for our fiducial model the evolution of the maximum toroidal, poloidal and total magnetic fields in the selected region until the bulk of the star starts to collapse and an apparent horizon is formed. The maximum total field in the full computational domain is also shown, which coincides with the local one after the magnetic field evolution has become nonlinear around 0.1 ms. This highlights the fact that the strongest magnetic fields in the entire computational domain are now to be found inside the selected region. While the poloidal component of the magnetic field remains essentially constant up to the collapse, the toroidal component is significantly amplified during the evolution. This is in contrast with previ-
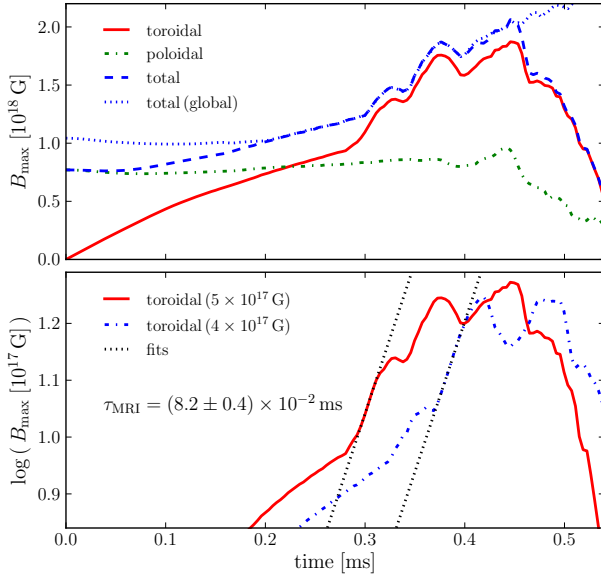
FIG. 2. *Top panel*: Evolution of maximum toroidal, poloidal and total magnetic fields in a selected region (see text) and of the maximum total field in the full computational domain (global), for $B_c^{in} = 5 \times 10^{17}$ G. *Bottom panel*: Toroidal field evolution in log scale for $B_c^{in} = 4$ and 5×10^{17} G. The dotted lines represent fits to the exponential growths with identical associated growth times τ_{MRI}.
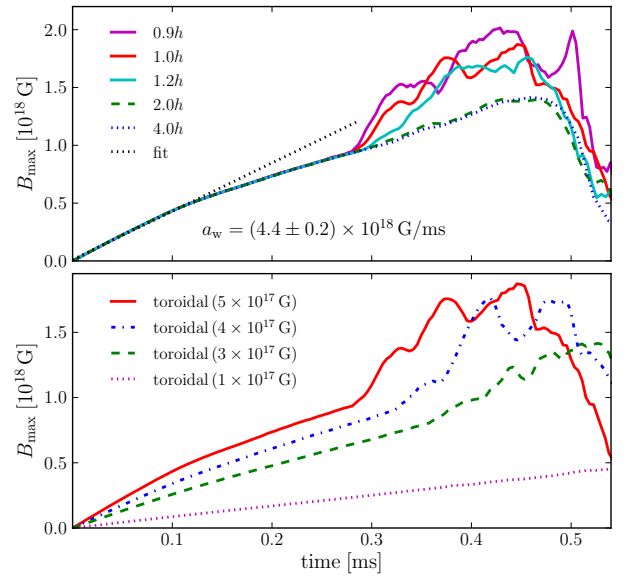
FIG. 3. *Top Panel*: Evolution of the maximum toroidal magnetic field in a selected region for $B_c^{in} = 5 \times 10^{17}$ G and different resolutions $(0.9 - 4.0)h$ (see text). The dash-dotted straight line is a fit to the initial linear growth stage of magnetic winding, common to all the simulations. *Bottom panel*: Same as top panel for fixed resolution h, but different B_c^{in}.

ous axisymmetric simulations [10, 16]. Initially, the toroidal field shows a linear growth due to magnetic winding, with a slope $a_{w,fit} = (4.4 \pm 0.2) \times 10^{18}$ G/ms that matches the value $a_w = (4.3 \pm 0.7) \times 10^{18}$ G/ms obtained by averaging the prediction of Eq. (1) in the region of interest (see also Fig. 3, upper panel). After ~ 0.3 ms, we distinguish two stages of exponential magnetic-field growth which coincide with the appearance of coherent channel-flow structures in the total magnetic field strength (the "ripples" in the top right panel of Fig. 1 and the top panel of Fig. 4). These are the characteristic signatures of the MRI found in local Newtonian axisymmetric simulations [14]. Note that the intermediate phase between the two growth periods coincides with the rearrangement of channel-flow structures. This can be seen in the upper portion of the upper panel of Fig. 4, and is reminiscent of the channel flow merging reported in [14] (see also [18]). Growth times τ_{MRI} associated with exponential rises in the toroidal field have been extracted for two different initial magnetic field strengths (cf. Fig. 2, lower panel). The values resulting from both fits agree within error bars and give $\tau_{MRI,fit} = (8.2 \pm 0.4) \times 10^{-2}$ ms. This is consistent with the analytic expectation that τ_{MRI} should be independent of the magnetic field strength. Furthermore, $\tau_{MRI,fit}$ is also in reasonable agreement with the values predicted by Eq. (2) for the selected region: $\tau_{MRI} \approx (4 - 5) \times 10^{-2}$ ms.

Figure 3 verifies additional important features of the MRI. The upper panel presents the maximum toroidal magnetic field in the selected region for the same initial data (with $B_c^{in} = 5 \times 10^{17}$ G) evolved using five grid resolutions ranging from $0.9h - 4.0h$ (with h referring to the fiducial grid spac-

ing of 44 m). For the two coarsest resolution runs ($2h$, $4h$), there are fewer than five grid points per λ_{MRI} (see below). The MRI therefore cannot be resolved in these cases. Increasing the resolution, we gradually recover the growth rate of the fiducial simulation. For the two finest resolutions ($0.9h$, $1.0h$), the extracted growth rates agree within error bars. Note that small differences in the maximum magnetic field after the rapid growth periods are expected when the resolution is changed. This is because with higher resolution we capture also smaller wavelengths, which couple nonlinearly and lead to slightly different magnetic-field amplifications. All of our runs recover the same expected magnetic winding behavior in the initial phase of the evolution.

The lower panel of Figure 3 illustrates the effect of varying the initial magnetic field strength at fixed grid resolution h. It validates the disappearance of the MRI when λ_{MRI} becomes too small compared with the resolution. Since $\lambda_{MRI} \propto k_{MRI}^i B_i \propto B_{pol}$ and the poloidal field strength B_{pol} remains approximately constant even during the MRI development (cf., upper panel of Fig. 2), the number of grid points per λ_{MRI} decreases as the initial magnetic field strength is lowered. At some point, the MRI can no longer be resolved. We detect a well-resolved instability only when $B_c^{in} > 3 \times 10^{17}$ G. The lower panel of Figure 3 also illustrates that increasing the initial magnetic field strength decreases the HMNS lifetime (this amounts to a factor $\gtrsim 2$ with respect to the non-magnetized case). This is due to more efficient outward transport of angular momentum which reduces the centrifugal support in the HMNS [9].

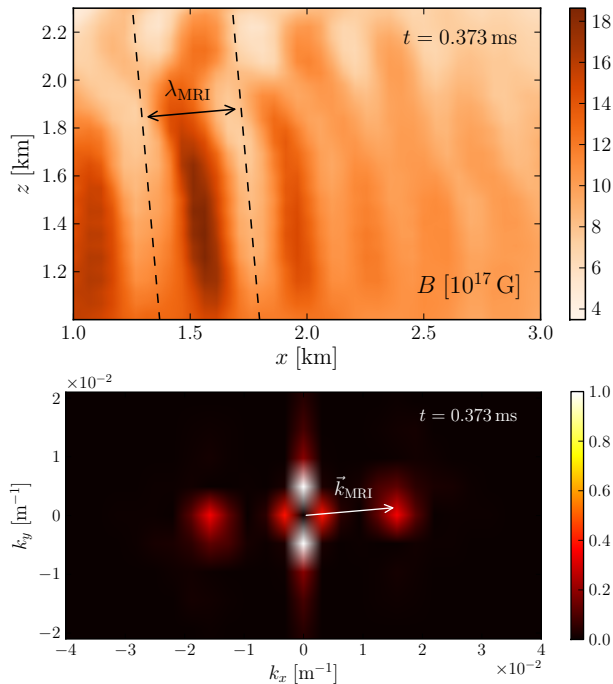The upper panel of Fig. 4 is a typical snapshot of the norm

FIG. 4. *Top Panel*: Norm of the total magnetic field in the selected region showing the fastest-growing MRI mode and the onset of the channel-flow merging (upper part). *Bottom panel*: Power spectrum showing a single dominant mode with $\lambda_{\mathrm{MRI}} \sim 0.4\,\mathrm{km}$.

of the magnetic field in the selected region after the MRI has fully developed ($t = 0.373\,\mathrm{ms}$). It illustrates the characteristic coherent channel-flow structures of the instability, which have not been observed in previous HMNS simulations, nor in global three-dimensional general-relativistic simulations. The clarity with which these structures emerge allows us to directly measure the wavelength of the fastest growing mode. The corresponding two-dimensional power spectrum is depicted in the lower panel of Fig. 4, which – apart from the maxima around the origin representing large-scale gradients over the selected region – clearly shows the presence of a single dominant mode k_{MRI}^i nearly parallel to the x-axis and corresponding to a wavelength of $\lambda_{\mathrm{MRI}} \approx 0.4\,\mathrm{km} \approx 9h$. Note that this geometry is different from the most commonly considered MRI scenarios where k_{MRI}^i is aligned with the

spin axis. There is not enough resolution in the Fourier domain to accurately measure the very small angle θ_{kx} between k_{MRI}^i and the x-axis, which varies slightly with time ($\theta_{kx} \approx 3° - 7°$). Using this range of values for θ_{kx}, the wavelength predicted by Eq. (2) for the region of interest is $\lambda_{\mathrm{MRI}} \approx (0.5 - 1.5)\,\mathrm{km}$, which is in good agreement with the measured value. It should be emphasized that the analytical estimates of Eq. (2) arise from a number of simplifying assumptions such as: Newtonian physics, axisymmetry, near-equilibrium and the short-wavelength approximation. None of these assumptions are strictly valid in our simulations. Notwithstanding the good agreement between our measurements and Eq. (2), a better analytic description of the MRI is needed for relativistic compact objects.

Conclusions. By performing global three-dimensional MHD simulations of HMNSs, we have observed the emergence of coherent channel-flow structures which provide direct evidence for the presence of the MRI in these systems. This is further supported by the verification of the main properties of the MRI expected from previous Newtonian analytical and numerical studies in other astrophysical scenarios. We note that the persistence of these structures is non-trivial as they may be unstable in three dimensions as a result of non-axisymmetric parasitic instabilities of the Kelvin-Helmholtz type [14, 24].

Showing the presence of the MRI in HMNSs is of great importance as the instability amplifies magnetic fields exponentially and can thus rapidly build up the very high magnetic-field strengths needed to launch a relativistic jet. Our results show that this amplification would already occur in the pre-collapse phase without having to wait for the torus to be formed after black hole creation. The dynamics in the torus can also amplify magnetic fields efficiently, but at much later times [11]. The amplification of magnetic fields in the HMNS due to the MRI is less than one order of magnitude in our model. However, the HMNS considered here is very short-lived even in the absence of magnetic fields [9]. In longer-lived HMNSs, the MRI could well reach several e-foldings and thus be a key ingredient in building the physical conditions necessary for launching the relativistic jet as revealed by the observations of SGRBs.

[1] V. Velikhov, Sov. Phys. JETP **36**, 995 (1959); S. Chandrasekhar, Proc. Natl. Acad. Sci. **46**, 253 (1960); S. A. Balbus and J. F. Hawley, Astrophys. J. **376**, 214 (1991).

[2] S. A. Balbus and J. F. Hawley, Reviews of Modern Physics **70**, 1 (1998); S. A. Balbus, Annu. Rev. Astron. Astrophys. **41**, 555 (2003); P. J. Armitage, Annu. Rev. Astron. Astrophys. **49**, 195 (2011).

[3] S. Akiyama, J. C. Wheeler, D. L. Meier, and I. Lichtenstadt, Astrophys. J. **584**, 954 (2003); A. Burrows, L. Dessart, E. Livne, C. D. Ott, and J. Murphy, Astrophys. J. **664**, 416 (2007).

[4] T. A. Thompson, E. Quataert, and A. Burrows, Astrophys. J. **620**, 861 (2005).

[5] H.-T. Janka, Annu. Rev. Nucl. Part. Sci. **62**, 407 (2012).

[6] M. Shibata, K. Taniguchi, and K. Uryū, Phys. Rev. D **71**, 084021 (2005).

[7] L. Baiotti, B. Giacomazzo, and L. Rezzolla, Phys. Rev. D **78**, 084033 (2008).

[8] V. Paschalidis, Z. B. Etienne, and S. L. Shapiro, Phys. Rev. D **86**, 064032 (2012).

[9] B. Giacomazzo, L. Rezzolla, and L. Baiotti, Phys. Rev. D **83**, 044014 (2011).

[10] M. D. Duez, Y. T. Liu, S. L. Shapiro, and M. Shibata, Phys. Rev. D **73**, 104015 (2006).

[11] L. Rezzolla, B. Giacomazzo, L. Baiotti, J. Granot, C. Kouveliotou, and M. A. Aloy, Astrophys. J. **732**, L6 (2011).

[12] M. Shibata, M. D. Duez, Y. T. Liu, S. L. Shapiro, and B. C. Stephens, Phys. Rev. Lett. **96**, 031102 (2006); K. Kiuchi, K. Kyutoku, and M. Shibata, Phys. Rev. D **86**, 064008 (2012).

[13] J. F. Hawley and S. A. Balbus, Astrophys. J. **400**, 595 (1992).

[14] M. Obergaulinger, P. Cerdá-Durán, E. Müller, and M. A. Aloy, Astronomy and Astrophysics **498**, 241 (2009).

[15] Y. Masada, T. Takiwaki, K. Kotake, and T. Sano, Astrophys. J. **759**, 110 (2012).

[16] M. D. Duez, Y. T. Liu, S. L. Shapiro, M. Shibata, and B. C. Stephens, Phys. Rev. Lett. **96**, 031101 (2006).

[17] M. Shibata, Y. T. Liu, S. L. Shapiro, and B. C. Stephens, Phys. Rev. D **74**, 104026 (2006); M. Obergaulinger, M. A. Aloy, and E. Müller, Astronomy and Astrophysics **450**, 1107 (2006); M. Obergaulinger, M. A. Aloy, H. Dimmelmeier, and E. Müller, Astron. Astrophys. **457**, 209 (2006).

[18] P. Cerdá-Durán, J. A. Font, L. Antón, and E. Müller, Astron. Astrophys. **492**, 937 (2008).

[19] B. Giacomazzo, L. Rezzolla, and N. Stergioulas, Phys. Rev. D **84**, 024022 (2011).

[20] N. Stergioulas and J. L. Friedman, Astrophys. J. **444**, 306 (1995).

[21] B. Giacomazzo and L. Rezzolla, Classical Quantum Gravity **24**, S235 (2007).

[22] D. Pollney, C. Reisswig, L. Rezzolla, B. Szilágyi, M. Ansorg, B. Deris, P. Diener, E. N. Dorband, M. Koppitz, A. Nagar, and E. Schnetter, Phys. Rev. D **76**, 124002 (2007).

[23] E. Schnetter, S. H. Hawley, and I. Hawke, Classical Quantum Gravity **21**, 1465 (2004).

[24] J. Goodman and G. Xu, Astrophys. J. **432**, 213 (1994).